ON THE DEVELOPMENT OF MESH GENERATION GUIDELINES FOR EFFICIENT FLOW SIMULATION OVER HIGH-LIFT DEVICES

Alexandre P. Antunes, ap-antunes@uol.com.br
Instituto Tecnológico de Aeronáutica, 12228-900 São José dos Campos, SP, Brasil

Ricardo Galdino da Silva, ricardo.galdino@poli.usp.br
Universidade de São Paulo, 05508-900 São Paulo, SP, Brasil

João Luiz F. Azevedo, joaoluiz.azevedo@gmail.com
Instituto de Aeronáutica e Espaço, CTA/IAE/ALA, 12228-903, São José dos Campos, SP, Brasil

Abstract. *The paper presents three-dimensional simulations over a trapezoidal wing with a single slotted flap and a slat, which was a model developed in order to provide a database for CFD validation. This semi-span model has been tested both in the NASA Ames 12-Foot Pressurized Tunnel (PWT) and the NASA Langley 14 by 22 Foot Subsonic Wind Tunnel (SWT). The simulations are performed for two flaps deflections, 20 and 25 degrees, and a few angles of attack; the slat deflection is hold constant at 30 degrees. Different mesh methodologies such as hexahedral meshes, and hybrid prismatic-tetrahedral meshes are used to perform the numerical simulations. Moreover, in order to observe the accuracy of the obtained aerodynamic coefficients, with respect to the mesh refinement and the turbulence model, additional simulations are performed. These aditional simulations are accomplished using the Sparlat-Allmaras turbulence model and the Menter SST turbulence model. The baseline grids range from 7.2 million to 12.8 million cells, while the finner grids are around 23 million cells.*

Keywords: *Computational Fluid Dynamics, High-Lift Devices, Aerodynamic Design*

1. INTRODUCTION

Computational Fluid Dynamics (CFD) has been consolidated as a quite mature science along the last thirty years of development (Johnson and Tinoco, 2005), (Vos et al., 2002). Nowadays, CFD is a well-know technology, deeply inserted into aerodynamic groups to perform the most diverse types of analyses. The paper will present three-dimensional simulations over a trapezoidal wing with a single slotted flap and a slat (Chaffin and Pirzadeh, 2005), (NASA, 2009). The model was developed in order to provide a database for CFD validation (Johnson, Jones, and Madson, 2000). The simulations are performed for two flaps deflections, 20 and 25 degrees, and a few angles of attack; the slat deflection is hold constant at 30 degrees. Different mesh methodologies such as hexahedral meshes, and hybrid prismatic-tetrahedral meshes are used to perform the numerical simulations. Moreover, in order to observe the accuracy of the obtained aerodynamic coefficients, with respect to the mesh refinement and the turbulence model, additional simulations are performed. These aditional simulations are accomplished using the Sparlat-Allmaras turbulence model and the Menter's SST turbulence model. The baseline grids range from 7.2 million to 12.8 million cells, while the finner grids are around 23 million cells.

The high-lift devices are intrinsically complex lifting components, that generate flow patterns with a vast range of physical phenomena (van Dam, 2002), (Payne et al., 2000), (Rogers et al., 2000). On such devices, one can commonly find boundary layer confluence, sonic regions, detached regions, flow relaminarization, among other phenomena. In Fig. 1, one can observe the complex flow structures generated by the airplane high-lift devices in a landing configuration. The capability to numerically capture all these physical phenomena, in tiny details, provides confidence on the obtained aerodynamic coefficients. This accuracy is a very important subject during the definitions of the high-lift systems due to the target design requirements that must be achieved to avoid penalties on the airplane performance (Eliasson, 2003), (Rudnick, 2003).

In order to achieve the target design requirements, a combination of several sets of leading-edge and trailing-edge high-lift systems can be used. For the leading-edge, one can choose which device is more appropriate among the following possibilities: hinged leading edge, variable camber leading edge, fixed slot, simple Krueger flap, folding, bull-nose Krueger flap, two-position slat, three-position slat. In a similar fashion, a large amount of possibilities is available for the trailing-edge devices, for instance: split flap, plain flap, simple slotted flap, fixed vane/main double slotted flap, main/aft double-slotted flap, triple-slotted flap. The combination of each one of these devices leads to different weight, cost, reliability, faring drag, and fairing blockage, thus, resulting in different stall characteristics.

From the fifties' to the seventies', the increase in the complexity of high-lift devices was the tendency (Flaig and Hilbig, 1993). However, in the late seventies', the beginning of CFD use allowed a way to decrease the high-lift device complexity by means of shape and gap/overlap optimization. This constantly search for simple high-lift devices is a natural consequence of the desire to decrease the direct operating cost, DOC, of the airplane. The high-lift devices have a substantial contribution to the airplane's DOC, and the capacity to accurately predict the aerodynamic coefficients, of

such configurations, is the cutting edge technology that allows the design of less complex devices. This capacity has an commercial implications in the competition between the airplane manufacturers, and, for this reason, there is not available experimental results for the numerical validation of a complete airplane with the high-lift devices deployed.

Figure 1. Numerical simulation over a commercial airplanes with the high-lift devices deployed.

The objectives of this investigation is to generate basic guidelines to accurately capture the lift and the drag coefficients for commercial airliner with high-lift configurations. Usually, for the high-lift configuration of an airplane, the drag coefficient, C_D, is not so well capture as the lift coefficient, C_L (Rumsey and Rivers, 2005). The proposed statement is sustained by a number of works performed by many other authors, and this study also intends to verify this behavior.

In order to generate these guidelines to capture the aerodynamic coefficients, it is necessary to perform studies with a simplified representative geometry. The main reason for such approach relies on the fact that, the simulation for a complete airliner demands a higher amount of computational resources and no validation is available, as mentioned before. Hence, a simpler trapezoidal wing with high-lift devices is taken as the main subject of study in the present work. Moreover, because this configuration is also publicly available this facilitates the reporting of the obtained results.

2. TRAPEZOIDAL WING MODEL WITH BODY POD

A trapezoidal wing model has been tested both in the NASA Ames 12-Foot Pressurized Tunnel (PWT) and the NASA Langley 14 by 22 Foot Subsonic Wind Tunnel (SWT) as part of the Advanced Subsonic Technology (AST) High-Lift Program, and the Advanced Subsonic Technology (AST) Airframe Noise Program. A considerably large number of high-lift device configurations and deflections was tested to produce the necessary experimental data for validation and development of CFD methods. Figure 2 shows some geometrical details from one of the tested configurations.

Three different configurations are adopted in order to perform the present study, one with a partial span flap and the others with a full span flap. These selected configurations are identified as *one*, *eight* and *nine*, according to the definition of the NASA configuration control matrix. The slat and flap deflections, for the above mentioned configurations, are respectivelly described below. For further details about the gap/overlap, the interested reader is directed to NASA (2009).

- Full Span Flap - Slat 30° and Flap 25°;
- Full Span Flap - Slat 30° and Flap 20°;
- Partial Span Flap - Slat 30° and Flap 25°.

In order to perform the first set of simulations, hybrid tetrahedral/prismatic meshes were generated over the adopted configurations. The generated meshes have a spherical outside boundary, which is located fifty chords away from the model. Since no wall boundary condition is imposed on the outer boundary, it is not necessary to reproduce in detail the wind tunnel test section. At this outer boundary of the mesh, the characteristic equations are imposed as boundary conditions. At mesh symmetry plane, the symmetry boundary condition is imposed. It worth to mention that the experimental results are corrected to eliminate the effect of the tunnel wall boundary layer over the aerodynamic coefficients of the configuration. Thus, the application of the above mentioned boundary conditions are appropriate for the performed simulations.

The hybrid baseline meshes, for the three configurations, have 9.8 million, 7.3 million, and 12.8 million cells, respectively. In Fig. 3, one can see the baseline surface meshes for configurations *one* and *nine*. The prismatic mesh layer is generated over the model surface using a geometric law with a growth ratio of 1.15. Moreover, the non-dimensional wall distance, Y^+ is set equal to one, by adjustments on the distance of the first point outside the wall. This distance is defined

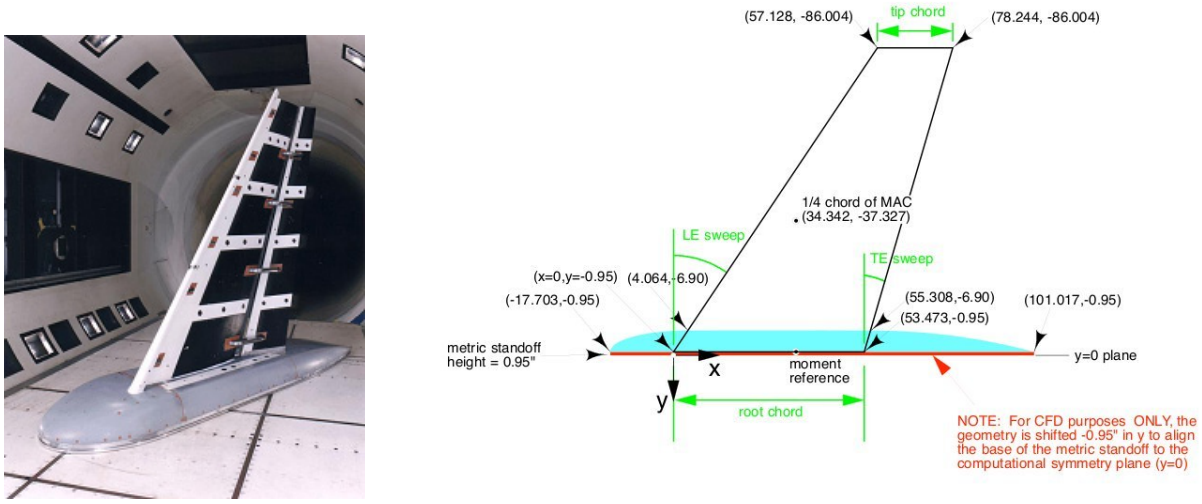

(a) Wing tunnel test section.

(b) Details of the wing planform.

Figure 2. NASA wind tunnel and trapezoidal wing model.

based on the flight condition and the expected shear stresses on the surface. The Y^+ for a wall-bounded flow can be defined in the following way,

$$y^+ \equiv \frac{u_* \, y}{\nu} \tag{1}$$

where u_* is the friction velocity at the nearest wall, y is the distance to the nearest wall and ν is the local kinematic viscosity of the fluid.

In particular, the generated hybrid baseline meshes have in common the fact that, at the trailing edge, there is only one cell face. In order to observe the effect of the trailing edge refinement on the obtained aerodynamic coefficients, mainly in the C_D coefficient, a refined mesh was generated over configuration *nine*. In this case, the trailing edge of the configuration *nine* is represented by three cell faces instead of just one. Although it seems a small change, the overall size of the mesh greatly increases. It goes from 12.8 million cells to 22.3 million cells.

Another set of simulations is performed using the hexahedral mesh methodology. Here, the main objective is to perform comparisons between the aerodynamic coefficients obtained by the hexahedral mesh and those obtained by the hybrid mesh. In order to accomplish the necessary simulations for the mesh methodology comparisons, two hexahedral meshes are generated over configuration *one*. The first one with 12 million cells, and the second one with 22.8 million cells. One can see in Fig. 4 the less refined hexahedral mesh. In both cases the mesh distribution along the direction normal to the surface follows a geometric law, with a growth ratio of 1.15. The first point outside the wall is also adjusted to have a Y_{plus} of one. Figure 5 shows a station cut over the less refined hexahedral mesh at the mid-station in the spanwise direction of the model wing. The comparison of results obtained with hexahedral and tetrahedral/prismatic meshes can provide some insight on the required mesh size for the hybrid and the hexahedral methodologies in order to better capture the aerodynamic coefficients.

3. METHODOLOGY

The simulations were performed with the CFD++ commercial package (Metacomp, 2010). All the results were obtained using the Reynolds-averaged Navier-Stokes equations, RANS. Moreover, the Spalart-Allmaras (1992) or the Menter SST turbulence models (Menter, 1993) were adopted in order to conduct a sensitivity study of the effects of the turbulence modeling on the final aerodynamic solutions. In the present case, only the test conditions adopted at the NASA Langley 14 by 22 ft Subsonic Wind Tunnel (SWT) are used to perform the numerical simulations. These conditions are freestream Mach number of 0.20 and Reynolds number of 4.3 million, based on the model mean aerodynamic chord.

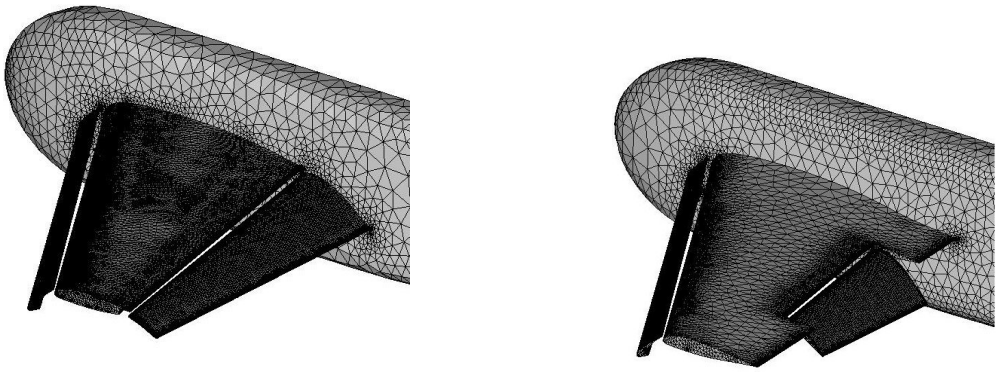

Figure 3. Surface mesh for configuration *one* and *eight* (hybrid mesh).

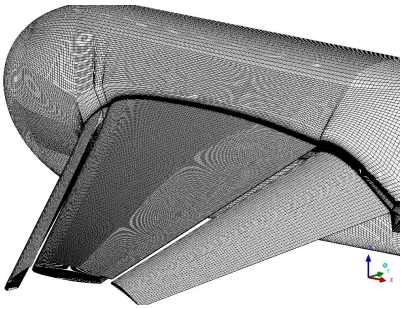

Figure 4. Surface mesh for configuration *one* (hexahedral mesh) .

4. RESULTS

4.1 Configuration One

In Fig. 6, one can observe the AOA versus C_L curves obtained by the simulations performed with the hybrid mesh, and the two hexahedral meshes. These simulations were accomplished using both SA and SST turbulence models for the hexahedral meshes, and only the SA turbulence model for the hybrid mesh.

The results presented by the hybrid mesh, have the stall angle of attack and the C_{Lmax} values below to the experimental results, and the curve is considerably shifted with respect to the experimental one. However, the C_{L_0} and the angular coefficient presented a reasonable correlation with the experimental data. Based on the authors' experience it was not expected to obtain such discrepancy with respect to the lift coefficient over the entire range of AOA. Usually, the mismatch occurs on the regions near the stall angle of attack.

One can see in Fig. 6 that the numerical results obtained with the hexahedral meshes, using the SA turbulence model, does not present such a shifted curve as the obtained by the hybrid mesh. Although these new results were able to reproduce the stall angle of attack, the C_{Lmax} value is undepredicted either. Moreover, one can not observe any difference

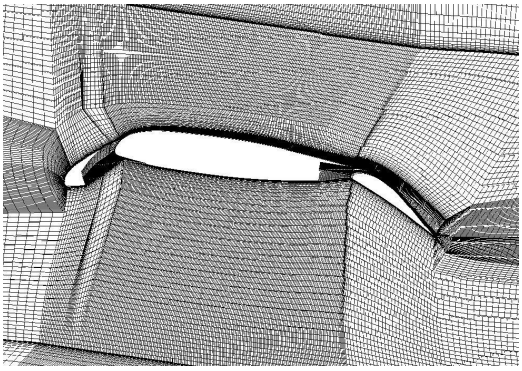

Figure 5. A station cut over the less refined hexahedral mesh.

between the results of the baseline and the refined meshes up to 24 deg. , which consists the linear part of the curve. Above this angle of attack the diference between the two meshes does not exceed 0.04 in terms of the C_L coefficient. Typically, at higher angles of attack, the nonlinearities of the flowfield are more pronounced, thus., refined meshes are more adequate to better capture such nonlinarities.

The numerical simulations performed with the same hexahedral meshes, but now with the SST model, in fact shows a small improvement in the quality of the obtained results. The linear part of the curve now has a perfectly match with the experimental results. Therefore, above this region, where the viscous effects are mandatory, the results presented the same lower C_{Lmax} value. One can notice again that, the difference between the baseline and the refined mesh just appears at higher angles of attack. As previously observed, the difference did not exceed 0.04 in terms of the C_L coefficient. The hexahedral baseline mesh presented results close to the refined mesh for both turbulence models, wich is an indication that the baseline mesh is already adequate for the intended simulations in the present case.

In terms of drag coefficient comparisons, one can see in Fig. 7 a mismatch of the hybrid mesh results with respect to the experimental results. The difference starts at 80 drag counts at C_L of 1.60 and reaches 450 drag counts near C_L of 2.70. Usually, the drag coefficient associated to the pressure component has a significant contribution on the overall computation of the total drag. The pressure drag contribution is typically negative at the trailing edge and, since the hybrid mesh only has one cell element along the trailing edge, it is quite possible that C_D is being overpredicted in the hybrid mesh calculations for this case. The results obtained with the hexahedral meshes, once again, show a better adherence to those from the experimental data. The SA turbulence model provided the right C_D for a lower C_L value, while the SST turbulence model provided the lower C_D coefficient with a right C_L value. Hence, there is a indication that if the C_L value increases the C_D coefficient obtained with the SA model would increase as well. Nevertheless, near the stall anlge of attack, one can see a small difference in C_D in Fig. 7, which is probably caused by the fact that the C_L values were slightly underpredicted at the stall condition. The explanation, at the present time, that such differences in the hexahedral mesh calculations come about because the current calculations are indicating more flow separation, at the flight condition in question, than the actual experiments. Hence, one would have less C_L, but more C_D.

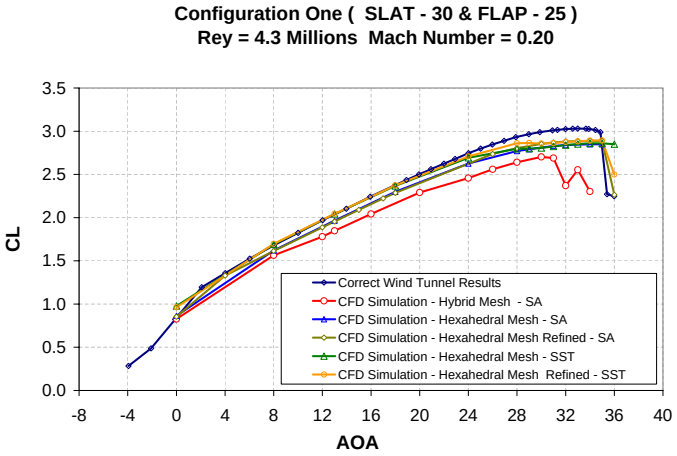

Figure 6. AOA versus CL for configuration *one*.

Figure 8 and Fig. 9 show an isometric view of the shear lines at different angles of attack. These shear lines are relative to the simulations performed with the hybrid mesh and the baseline hexahedral mesh, using the SA turbulence model. It can be noticed that, at zero angle of attack, the flow pattern obtained with both baseline hexahedral and hybrid meshes is pretty similar. There is a massive separated region over the flap upper surface, as well as a vortex region at the flap trailing edge near the pod junction. At lower angles of attach, it is very common to have this separated flow region over the high-lift devices. As the angle of attack increases, the flowfield pattern captured by both mesh methodologies become considerably different. The hexahedral mesh shows a constant separated flow region on the flap-pod junction, for angles of attack up to 28 deg. On the other hand, the results obtained with the hybrid mesh show that the flap-pod separated region disappears at angles of attack higher than 8 deg. Moreover, the hybrid mesh shows a separated flow area on the pod element, which is not present in the hexahedral mesh. Hence, one can notice how different the obtained results can be as a function of the adopted mesh methodologies and the spatial discretization.

Part of this discrepancy can be attributed to the horseshoe vortex present at the region near the leading edge of the slat, as one can see in Fig. 10. Usually, whenever a surface is mounted into another base surface with a substantial angle between them, such as the slat and the pod surfaces, it is possible to have the apperance of such vortical structures. This vorticity affects the upstream flowfield, the downstream flowfield and the shear lines over the body. Moreover, it makes the accurate capture of the aerodynamic coefficients a challenging task. Since the hexahedral mesh has a more refined

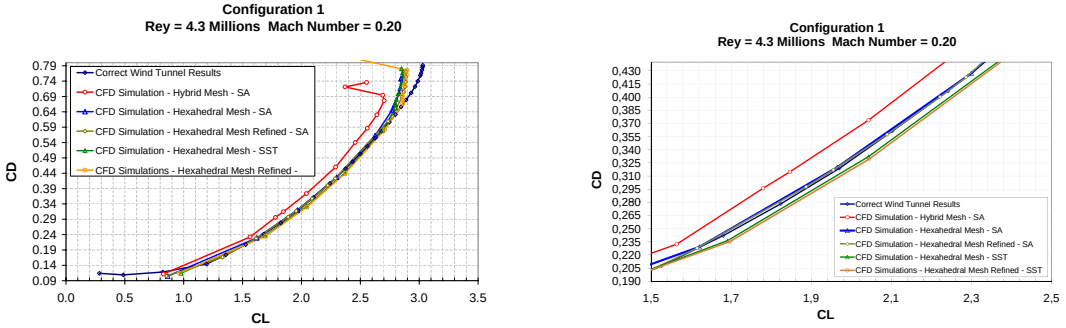

(a) CL versus CD ranging from 0.7 up to 2.8.

(b) CL versus CD ranging from 1.5 up to 2.5.

Figure 7. CL versus CD for configuration *one*.

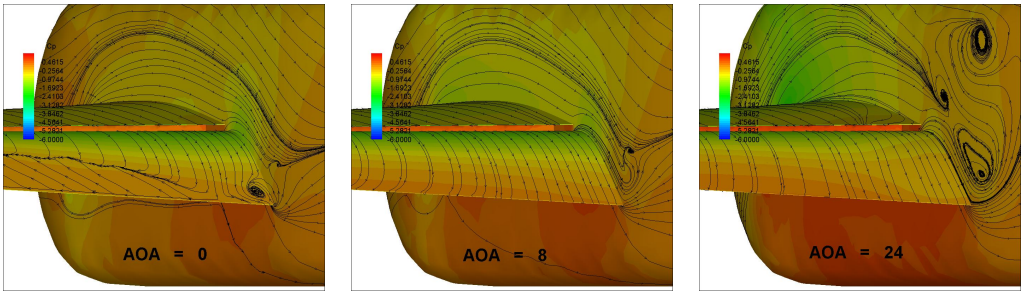

Figure 8. Shear lines over configuration *one* for three angles of attack - Hybrid Mesh.

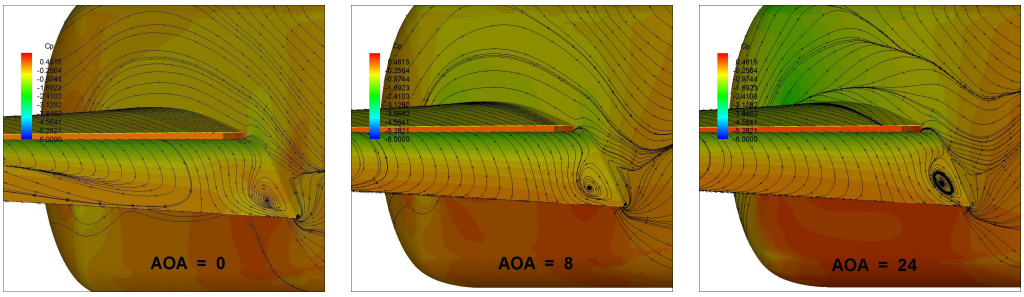

Figure 9. Shear lines over configuration *one* for three angles of attack - Hexahedral Mesh.

volumetric discretization, it can better capture the emanated vorticity from the upstream flowfield. In the hybrid mesh, the tetrahedra located beyond the prism layer present a rapid volumetric growth, which may cause some adverse effects in the capability of capturing such physical phenomena with accuracy. In Fig. 11 one can observe the vorticity capture at different planes along the x direction of the model for the $AOA = 20$ deg. These presented results are relative to the hexahedral mesh and it is pretty clear the vorticity generated at the wing tip, and at the trailling edge of the slat, main element, and flap devices. The vorticity emanated by the slat component can be identified initially in Fig. 11, at the plane $Y = 1.350$, as a blue spot over the flap region. This vorticity is diffused along the x direction, and in a certain moment it merges with the main element and flap vorticity. Indeed, these low pressure region affects the shear lines over the body and eventualy the flow dettachment in certain regions over the wing.

In Fig. 12 one can observe the comparison between the experimental and the numerical pressure distribution, Cp, at the mid station along the spanwise direction. In general terms all the pressure peaks were able to be adequately captured. The slat pressure distribution presents the most pronouced difference with respect to the experimental results, the distribution seems to be a little bit distorted. The main element has the better fit and the flap distribution shows a kink at the leading edge. This kink might be connected to some aerodynamic effect provoked by the main element cove, or even to some numerical aspect of the mesh generation process. The authors' are investigating the possible reason associated with this phenomena.

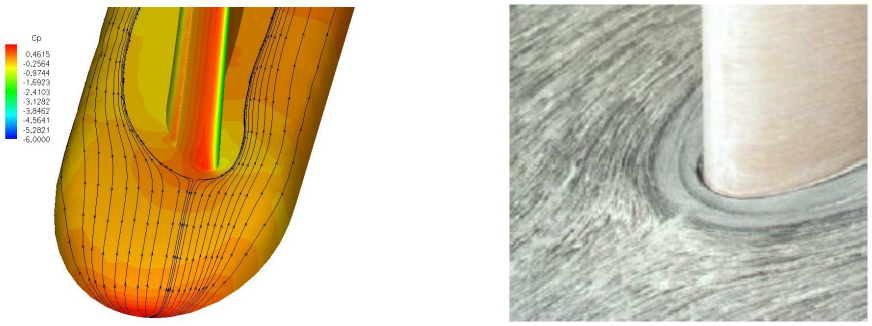

(a) Horseshoe vortex emitted from the slat leading edge region.

(b) Example of an experimental oil visualization of the leading edge horseshoe vortex.

Figure 10. Horseshoe vortex emitted from the slat leading edge region.

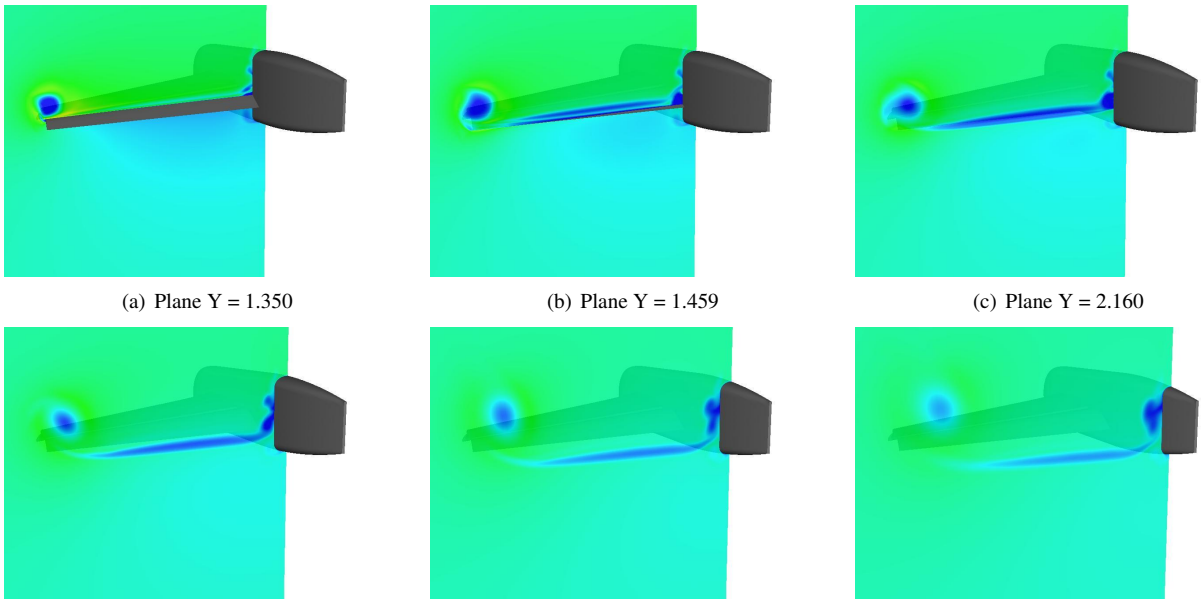

(a) Plane Y = 1.350 (b) Plane Y = 1.459 (c) Plane Y = 2.160

(d) Plane Y = 2.380 (e) Plane Y = 2.600 (f) Plane Y = 2.740

Figure 11. Velocity contours showing regions of low pressure downstream of the wing.

4.2 Configuration Eight

The simulations performed for configuration *eight* used only the hybrid baseline mesh. In Fig. 13, one can observe the AOA versus C_L curve obtained from the simulations. The wind tunnel results do not contain corrected data information up to the stall angle of attack. For this reason, one cannot observe the experimental results at the stall angle of attack.

One can notice that there is a discrepancy in relation to the experimental results, in a very similar way as observed for the hybric mesh calculations for configuration *one*. This difference is less pronounced due to the lower flap deflection in the present case. Lower flap deflections generate smaller aerodynamic spanwise loading. Thus, the vortex near the slat leading edge has a lower circulation intensity. If the discrepancies can be attibuted to the inability of accurately capturing the effect of this vortex, as it was stated, the decrease in this structure intensity leads to a less disturbed downstream flowfield. Therefore, the simulation can better capture the aerodynamic coefficients.

In Fig. 13, one can see the C_D versus C_L curve. Here, one can notice that the same shift, observed for configuration *one* is also present, therefore, not so pronounced. In Fig. 14, one can observe the shear lines for this configuration at two different angles of attack, 12 and 16 deg. The flow pattern follows the same behavior observed for configuration *one*. Near the flap-pod junction, there is a separated flow region, that disappears at higher angles of attack. However, for this configuration, flow separation only disappears at 16 deg, whereas for configuration *one* it disappears at 8 deg. angle of attack.

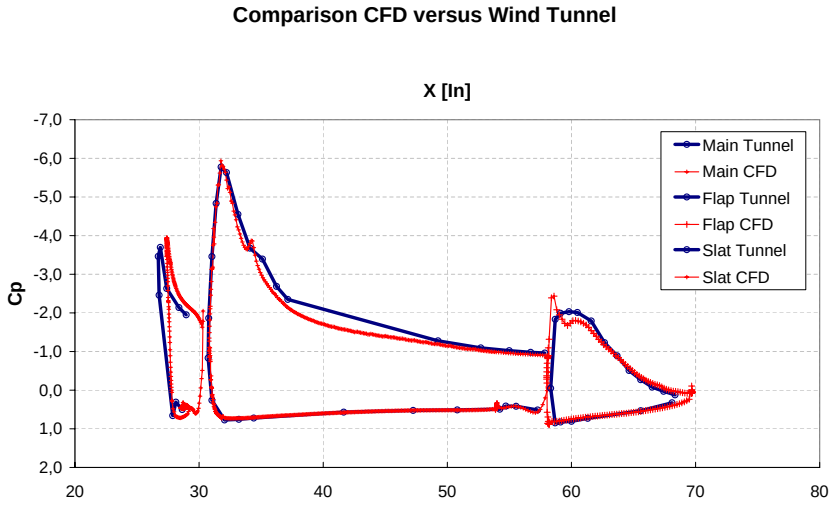

Figure 12. Profile Cp distribution at the mid-station along the span.

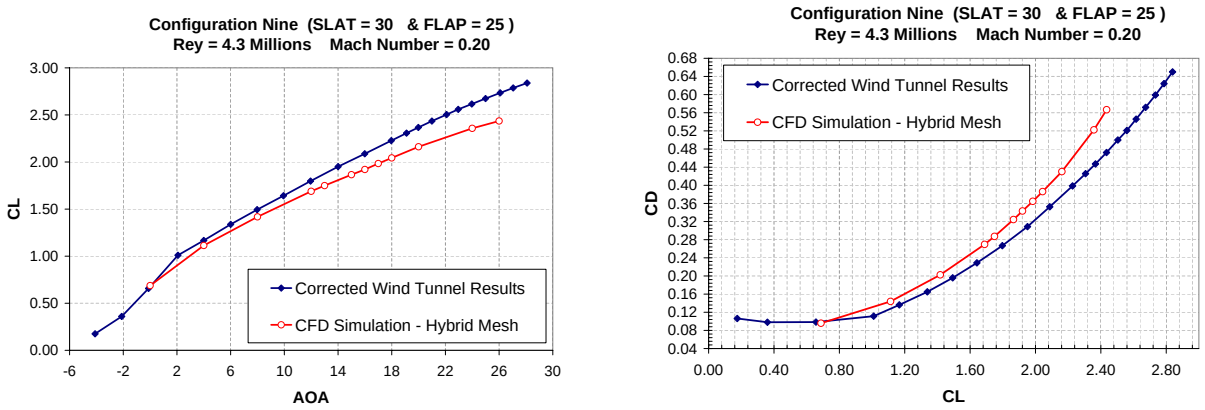

(a) AOA versus CL. (b) CL versus CD.

Figure 13. Aerodynamic coefficients for configuration *eight*.

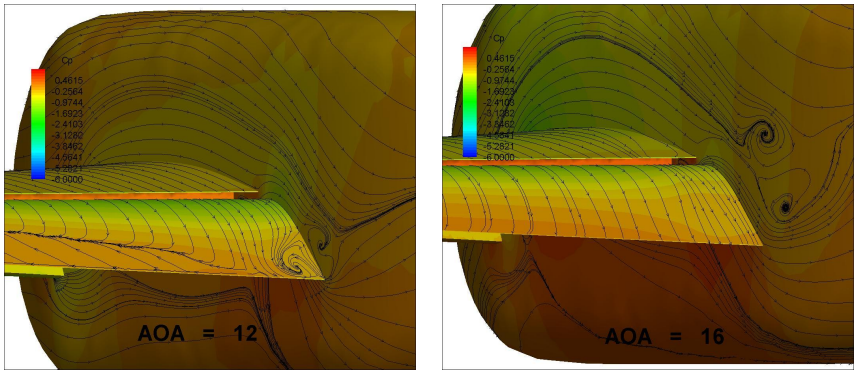

Figure 14. Shear lines over configuration *eight* for two angles of attack.

4.3 Configuration Nine

The simulations performed for this configuration used the baseline and the refined hybrid meshes. In Fig. 15, one can observe the shear lines for the baseline mesh of configuration *nine* at the following angles of attack, 0, 8, 20, and 28 deg. There is an important aspect that must be pointed out from Fig. 15, and which is the apperance of a small separated

region on the wing trailing edge near the wing-pod junction, at angle of attack of 8 deg. This separated region might be generated by the adverse pressure gradient at the trailing edge, as well as by an adverse effect caused by the upstream vorticity emanated from the slat leading edge. This small separated region propagates upstream as the angle of attack increases.

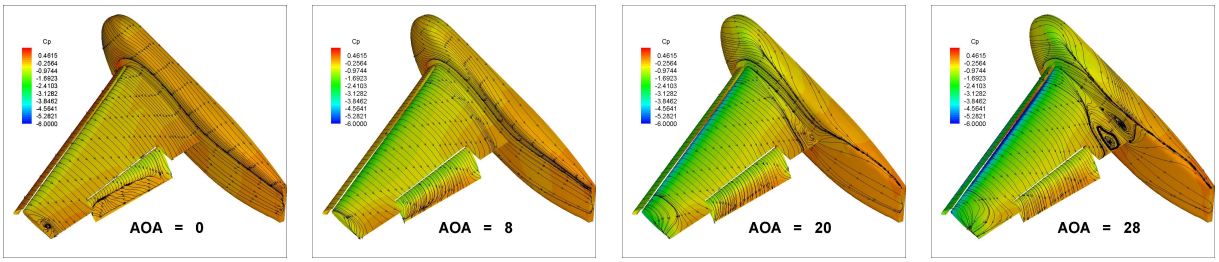

Figure 15. Shear lines over configuration *nine* for four angles of attack using the baseline mesh.

In Fig. 16, one can observe the AOA versus C_L curve. A good adherence is obtained until 12 deg. angle of attack for both meshes. Beyond this angle of attack, there is a mismatch between the numerical and the experimental results. Again, the discrepancy can be attributed to the inability of the present calculation procedure, with the meshes here used, of capturing with adequate acurracy the effect of the emanated vorticity from the slat leading edge. An interesting point here is the fact that, at lower angles of attack, a good matching between the experimental and the numerical coefficients is obtained, for all the three configurations, despite the separated regions over the high-lift devices.

It is also possible that, at lower angles of attack, the vorticity from the slat leading edge is being convected towards the lower surface of the model and, therefore, not disturbing the upper surface. At the lower surface, usually, there is no adverse pressure gradient, thus, the presence of the upstream vorticity might cause boundary layer thickening, and an increase in the C_D but not a separation of the flow. It should be pointed out, however, that the upper surface of the flap is always separated for such angles of attack. On the other hand, for the higher AOA, the upstream vorticity disturbes the flowfield on the upper surface, causing boundary layer thickening and distortion of the shear lines due to the low pressure core of the vortex. In this condition, the accurate capture of the aerodynamic coefficient is complicated.

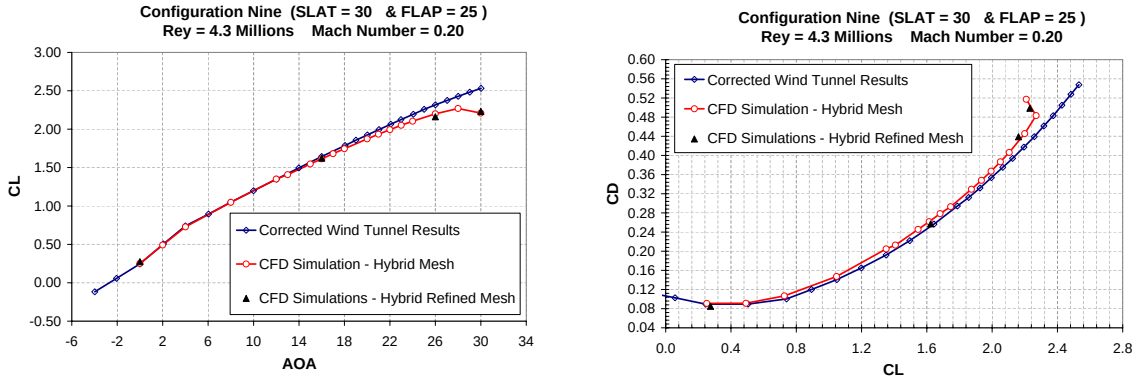

(a) AOA versus CL. (b) CL versus CD.

Figure 16. Aerodynamic coefficients for configuration *nine*.

The obtained results for the refined mesh did not produce any improvement in the calculated C_L coefficients. Although this mesh has more cells than the baseline mesh, mostly of the refinement is concentrated in the trailing edge of the wing. Hence, in terms of volumetric aspect, this mesh does not provide a better capability to capture the horseshoe vortex. Figure 16 shows a comparison in terms of drag coefficients between the numerical and the experimental results. It can be noticed that the shift is smaller than the observed for configurations *one* and *eight* for both simulations, *i.e.*, with the baseline and the refined meshes. The refined mesh does not present a better matching with the experimental results even for C_D, despite the fact that most of the refinement happened at the trailing edge. This is an indication that, although the mesh is more adequate to capture the pressure drag component at the trailing edge, the lack of a volumetric refinement does not allow the capture of the effect of the horseshoe vortex. Hence, the overall results are not improved.

5. CONCLUSIONS

The performed simulations for all the three configurations have shown a fairly good correlation with the experimental results up to the stall angle of attack. Nevertheless, the matching is not perfect and some discrepancies are readily observed in the results presented. The hexahedral mesh methodology, adopted for configuration *one*, has shown that this approach produces better results than those obtained with the hybrid mesh methodology. This conclusion is correct for both aerodynamic coefficients, C_L and C_D. In general, the hexahedral mesh methodology provides meshes with a lower number of cells and with a better volumetric discretization. In the authors' opinion, in order to have a hybrid mesh with the same accuracy of the hexahedral mesh, the number of elements in the hybrid mesh would need to be increased at least by a factor of 2.

The results obtained with configuration *nine* are closer to the experimental data, although the used mesh for the simulation is not hexahedral. Such behavior is possibly associated with a less intense horseshoe vortex for this configuration, because the flap is not extended to the wing-pod junction. The horseshoe vortex makes the capture of the aerodynamic coefficients a challenging task. In such case, a careful evaluation of the mesh characteristics is necessary. There is the need for developing very controlled meshes, in terms of point distributions and mesh spacings, and, also, mesh topologies which adequately allow capturing of the phenomena expected in the simulations.

6. ACKNOWLEDGEMENTS

The authors acknowledge the partial support of Conselho Nacional de Desenvolvimento Científico e Tecnológico, CNPq, under the Research Project Grant No. 312064/2006-3.

7. REFERENCES

Ansys Inc., ICEM-CFD ™, "<http://www.icemcfd.com/>" [visited 10 May 2010].

Chaffin, M., and Pirzadeh, S., 2005, "Unstructured Navier-Stokes High-Lift Computations on a Trapezoidal Wing," AIAA Paper No. 2005-5084, *23rd AIAA Applied Aerodynamics Conference*, Toronto, Canada.

Eliasson, P., 2003, "CFD Improvements for High-Lift Flows in the European Project EUROLIFT," AIAA Paper No. 2003-3795, *21st AIAA Applied Aerodynamics Conference*, Orlando, FL.

Flaig, A., and Hilbig, R., 1993, "High-Lift Design for Large Civil Aircraft," *High-Lift Systems Aerodynamics*, AGARD CP–515, pp. 31-1–31-12.

htpp://db-www.larc.nasa.gov/trapwing/archive/register/ [visited 20 Dec. 2009].

Johnson, P., Jones, K.M., and Madson, M., 2000, "Experimental Investigation of a Simplified 3D High-Lift Configuration in Support of CFD Validation," AIAA Paper 2000-4217, *18th AIAA Applied Aerodynamics Conference and Exhibit*, Denver, CO.

Johnson, T.F., and Tinoco, E.N., 2005, "Thirty Years Of Development and Application Of CFD at Boeing Commercial Airplane Seattle," *Computers & Fluids*, Vol. 34, No. 10, pp. 1115-1151.

Menter, F.R., 1993, "Two-Equation Eddy-Viscosity Turbulence Models for Engineering Applications," *AIAA Journal*, Vol. 32, No. 8, pp. 1598-1605.

Metacomp Technologies Inc., CFD++, "<http://www.metacomptech.com/>" [visited 20 May 2010].

Payne, F.M., Wyatt, G.W., Bogue, D.R., and Stone, R.C., 2000, "High Reynolds Number Studies of a Boeing 777-200 High-Lift Configuration in the NASA ARC 12' Pressure Tunnel and NASA LaRC National Transonic Facility," AIAA Paper 2000-4220, *18th AIAA Applied Aerodynamics Conference and Exhibit*, Denver, CO.

Rogers, S.E., Roth, K., Nash, S.M., Baker, M.D., Slotnick, J.P., Whitlock, M., 2000, "Computational of Viscous Flow for a Boeing 777 Aircraft in Landing Configuration," AIAA Paper No. 2000-4221, *18th AIAA Applied Aerodynamics Conference and Exhibit*, Denver, CO.

Rudnick, R., 2003, "CFD Assessment for High-Lift Flows in the European Project EUROLIFT," AIAA Paper No. 2003-3794, *21st AIAA Applied Aerodynamics Conference*, Orlando, FL.

Rumsey, C.L., and Rivers, S.M., 2005, "Study of CFD Variation on Transport Configurations from the Second Drag-Prediction Workshop," *Progress in Aerospace Sciences*, Vol. 34, No. 07, pp. 785-816.

Spalart, P.R., and Allmaras, S.R., 1992, "A One-Equation Turbulence Model for Aerodynamic Flows," AIAA Paper No. 92-0439, *Proceedings of the 30th AIAA Aerospace Sciences Meeting and Exhibit*, Reno, NV.

van Dam, C.P., 2002, "The Aerodynamic Design of Multi-Element High-Lift Systems for Transport Airplanes," *Progress in Aerospace Sciences*, Vol. 38, No. 2, pp. 101-114.

Vos, J.B., Rizzi, A., Darraq, D., and Hirschel, E.H., 2002,"Navier-Stokes Solvers in European Aircraft Design," *Progress in Aerospace Sciences*, Vol. 38, No. 8, pp. 601-697.

8. Responsibility notice

The author(s) is (are) the only responsible for the printed material included in this paper